Research Article

First- and second-order Raman spectra of carbonaceous material through successive contact and regional metamorphic events (Ryoke belt, SW Japan)

Etienne Skrzypek [a,b,*]

[a] *Department of Geology and Mineralogy, Graduate School of Science, Kyoto University, Kitashirakawa-Oiwakecho, Sakyo-ku, 606-8502 Kyoto, Japan*
[b] *Institute of Earth Sciences, NAWI Graz Geozentrum, Petrology and Geochemistry, University of Graz, Universitätsplatz 2, 8010 Graz, Austria*

ARTICLE INFO

ABSTRACT

The evolution of both the first- and second-order Raman spectra of carbonaceous material (CM) through successive contact and regional metamorphic events is explored in the western part of the Ryoke belt (Iwakuni-Yanai area, SW Japan). Thirty-two metasedimentary rock samples were collected along a N-S gradient locally affected by contact metamorphism *before* and *after* the main regional tectono-metamorphic event (DP1). First-order spectra document a decreasing peak area ratio R2 and an increasing temperature T_{CM} towards the south and the surrounding granitoids. Domains with intermediate (535–600 °C) T_{CM} values match the extent of the pre-DP1 contact aureole but also image a so far unclear post-DP1 aureole. The axial part of the belt, likely unaffected by granite intrusions, preserves southward increasing T_{CM} from 425 to 660 °C. Second-order spectra show a single S1 band that splits into two peaks (S1- and S1+) whose frequency difference ΔS1 increases stepwise towards the south. The spatial distribution of ΔS1 follows that of the E–W trending regional metamorphic zones. The splitting of S1 indicates a transition from two-dimensional to three-dimensional CM and occurs at ~500 °C, which seems to be common to all metamorphic belts worldwide. Despite regional metamorphism CM was able to record the post-DP1 contact overprint and there is no clear observation of delayed CM recrystallization, which likely depends on the crystallinity of the CM precursor. A discrepancy between first- and second-order Raman parameters suggests that they partly record the influence of different factors; R2 gives an account of thermal events, particularly those related to localized contact metamorphism, whereas ΔS1 potentially yields information on regional variations in heating duration and pressure. This demonstrates the potential of the full Raman spectrum of CM for deciphering the complex thermal history of orogenic systems.

© 2021 The Author(s). Published by Elsevier B.V. This is an open access article under the CC BY license (http://creativecommons.org/licenses/by/4.0/).

1. Introduction

Organic matter, if not fully decomposed in a near-surface environment, is buried together with other mineral detritus and incorporated into sedimentary rocks. Due to subsequent diagenesis and metamorphism this carbonaceous material (CM) will structurally and compositionally change from a C ± H ± N ± O ± S-bearing organic compound to eventually pure graphite (e.g. Buseck and Beyssac, 2014).

The transformation of CM with metamorphic grade has been investigated by chemical and X-ray diffraction (XRD) analyses (e.g. French, 1964; Grew, 1974; Griffin, 1967; Itaya, 1981; Izawa, 1968; Landis, 1971; Tagiri, 1981; Wang, 1989), transmission electron microscopy (e.g. Bénny-Bassez and Rouzaud, 1985; Beyssac et al., 2002b; Buseck and Huang, 1985; Buseck et al., 1987) or Raman spectroscopy (e.g. Pasteris and Wopenka, 1991; Wopenka and Pasteris, 1993). The latter

method allows in situ analysis of CM and provides information on CM crystallinity by means of the first-order spectrum (e.g. Knight and White, 1989; Pimenta et al., 2007; Tuinstra and Koenig, 1970), but also on three-dimensional ordering of CM thanks to the second-order spectrum (e.g. Beyssac et al., 2019; Cançado et al., 2008; Lespade et al., 1984; Wilhelm et al., 1998). A major advance related to this technique was that systematic changes in the first-order Raman spectrum of natural samples could be correlated with independent temperature estimates to derive a geothermometer (Beyssac et al., 2002a).

Thermometry based on Raman spectroscopy of carbonaceous material (RSCM) was calibrated using material from various geological settings. For the 330–650 °C temperature range, Beyssac et al. (2002a) used samples from worldwide belts affected by regional metamorphism while Aoya et al. (2010) relied on samples from contact metamorphic aureoles in Japan. The applicability of RSCM thermometry was extended to lower temperature (150–400 °C) by Rahl et al. (2005) with very-low-grade forearc metasediments, by Lahfid et al. (2010) with flysch sediments collected along a low-grade gradient, and by Kouketsu et al. (2014a)

with regionally metamorphosed low-grade metasedimentary rocks. The important aspect of all these calibrations is that they rely on originally non- to weakly-metamorphosed samples that were affected by a single heating event.

Orogenic systems are, however, commonly characterized by successive and partly overprinting thermal events (e.g. Brown, 1993). This led Delchini et al. (2016) to address the validity of RSCM thermometry in a complex setting, namely regionally metamorphosed Variscan metasediments overprinted by contact metamorphism. They concluded that RSCM analyses of samples previously affected by greenschist to amphibolite facies regional metamorphism can still reveal peak temperature conditions attained during a subsequent contact overprint. This view was recently challenged by Beyssac et al. (2019) who observed delayed CM recrystallization in the contact aureole of the Ballachulish Complex. They attributed "insufficient" CM recrystallization during contact metamorphism to CM pretexturation resulting from preceding regional metamorphism at ~500 °C, and consequently cautioned the use of RSCM thermometry in polyphase metamorphic terrains.

Rooted in an attempt at precisely constraining the thermal history of the plutono-metamorphic Ryoke belt (SW Japan), the present work evaluates the validity and usefulness of RSCM data in a polymetamorphosed terrain. This is done from the point of view of both the first- and second-order Raman spectra of CM, as the latter are only rarely explored and quantified (e.g. Beyssac et al., 2002a, 2019; Nakamura and Akai, 2013). Several decades of structural, petrological and geochronological investigations in the Ryoke belt have provided a comprehensive picture of its tectono-thermal evolution (see Wallis and Okudaira, 2016 for a synthesis). In the Iwakuni-Yanai area (western part of the Ryoke belt), the prominent feature preserved by metasedimentary rocks is a regional metamorphic gradient with increasing Pressure — Temperature ($P - T$) conditions from north to south (e.g. Brown, 1998). On its western flank granitoids generated contact metamorphism *before* the regional overprint, whereas on its eastern flank a later intrusion caused contact metamorphism *after* the regional event (e.g. Skrzypek et al., 2016). This field target therefore offers the opportunity to monitor the response of CM to intermingled contact and regional metamorphic events, and to evaluate the potential of CM for deciphering the thermal evolution of complex metamorphic belts.

2. Geological outline of the Iwakuni-Yanai area

The Ryoke belt exposed in the Iwakuni-Yanai area is composed of metasedimentary rocks intruded by numerous granitoids (e.g. Higashimoto et al., 1983; Fig. 1). It formed by polyphase deformation and metamorphism of Triassic to Jurassic accretionary-wedge sediments (Takami et al., 1993) during Cretaceous plutonic activity (e.g. Nakajima, 1994; Nakajima et al., 1990; Wallis and Okudaira, 2016). The metasedimentary rocks presently expose a low-*P*/high-*T* metamorphic gradient that increases from north to south (e.g. Brown, 1998) while the lithology evolves from low-grade (meta-) mudstone/sandstone to medium-grade schist and high-grade gneiss (Fig. 1). The surrounding biotite(±amphibole)-bearing granitoids show a dominantly I-type affinity (Nakajima et al., 2016) and belong to the ilmenite series of Ishihara (1977).

Two main deformation phases (DP) are recognized: the DP1 event generated the dominant subhorizontal foliation observed in the gneiss zone while DP2 produced km-scale upright folding in both the schist and gneiss zones (Okudaira et al., 1995; Skrzypek et al., 2016). Pre-DP1 contact metamorphism around the western granitoids is evidenced by the presence of pre-tectonic andalusite and cordierite blasts (Nureki, 1974; Skrzypek et al., 2016; Fig. 1). This was followed by a *syn*-DP1 overprint referred to as regional as it is associated with the growth of foliation-forming parageneses that are used to define E — W trending metamorphic zones (Fig. 1). From north to south Ikeda (1998) defined the chlorite, chlorite—biotite, biotite, muscovite—cordierite and K-feldspar—cordierite zones, with the higher-grade sillimanite—K-feldspar and

garnet—cordierite zones being outside the scope of the present study. Pressure — Temperature conditions – all implicitly ascribed to regional metamorphism – increase from ~450–500 °C/1 kbar in the Chl — Bt and Bt zones to 520–550 °C/1–2.5 kbar in the Ms. — Crd zone and 590–675 °C/1–3 kbar in the Kfs — Crd zone (Ikeda, 2004; Kouketsu et al., 2014b; Sugawara, 2013). Post-DP1 contact metamorphism is locally observed around the granitic intrusion in the eastern part of the study area (Fig. 1).

The western granitoids are pre-DP1 intrusions with U — Pb zircon and monazite ages of 105–100 Ma that constrain the first contact metamorphic event (Skrzypek et al., 2016, 2020). The southern granitoids comprise syn-DP1 gneissose granodiorite and porphyritic granite emplaced at 100–98 Ma (e.g. Okudaira et al., 1995; Skrzypek et al., 2016), and a post-DP1 quartz diorite emplaced at *c.* 94 Ma (e.g. Akasaki et al., 2015; Mateen et al., 2019). The post-DP1 eastern granite has a U — Pb zircon age of *c.* 96 Ma (Skrzypek et al., 2016), and is likely associated with microgranite dykes that are found within the metasedimentary belt and show similar U — Pb zircon ages of *c.* 96–94 Ma (Skrzypek et al., 2016; Fig. 1). The regional metamorphic event is thought to be coeval with DP1 deformation based on U — Pb dates of 103–97 Ma obtained from metamorphic zircon domains in gneiss samples from the highest grade Grt — Crd zone (Nakajima et al., 2013; Skrzypek et al., 2016). However, monazite dating by different methods provides dates as young as 89 ± 5 Ma in the Kfs — Crd zone (Skrzypek et al., 2018). Recrystallized domains in magmatic monazite from a western granitoid sample yield U — Pb dates between 102 and 91 Ma and similarly suggest the persistence of medium- to high-*T* conditions until *c.* 90 Ma (Skrzypek et al., 2020).

3. Samples

Thirty-two samples were collected from the Chl — Bt to the Kfs — Crd zone (Fig. 1). The rock types comprise weakly metamorphosed mudstone, dark schist, spotted schist, massive hornfels, gneiss and metachert (Fig. 2). The samples can be broadly classified as pelitic, psammitic or siliceous metasediments based on the relative proportions of micas and quartz in thin section. Several samples show features suggesting a contact metamorphic overprint such as mm-scale muscovite or biotite laths, and andalusite or cordierite porphyroblasts (~0.5 cm) (Fig. 2c).

Schistose rocks are fine-grained and preserve the original sedimentary bedding defined by alternating mica- and quartz-rich layers. Micas (Ms ± Bt) grow parallel to the bedding planes and locally define an oblique, spaced cleavage resulting from DP2 folding (Fig. 2b). Gneissose rocks are coarser-grained and exhibit a pervasive metamorphic foliation defined by the alternation of quartz±plagioclase- and biotite-rich layers (Fig. 2e). Pelitic samples correspond to black schist or mica-rich gneiss with relatively abundant CM distributed across the entire thin section (Fig. 2c). Psammitic samples contain thicker Qtz ± Pl-rich layers, and the less abundant CM is mainly present in the mica-rich layers (Fig. 2b). Siliceous samples appear as white or greyish banded metachert at the macroscopic scale; under the microscope they show thick Qtz-rich layers separated by thin mica-rich bands where most of the overall scarcely present CM is observed (Fig. 2d). In all samples CM is dominantly found inside or along the boundaries of the main matrix minerals (Qtz, Ms., Bt, Pl; Fig. 3). Carbonaceous material also forms well-defined inclusion trails in andalusite and cordierite porphyroblasts when present (Fig. 3).

Four different CM textures (I-IV) are distinguished under the microscope. Type I corresponds to a dusty texture of fine-grained, scattered CM particles that are only locally connected to form thin, discontinuous layers (Fig. 3a, b). This texture is observed in low-grade and CM-poor rocks (6 samples). Type II involves fibers and elongated grain clusters of variable thickness that form continuous layers (Fig. 3c, d). Type II is common in schistose, CM-rich lithologies (10 samples). Type III texture is represented by relatively small, scattered grains with an irregular
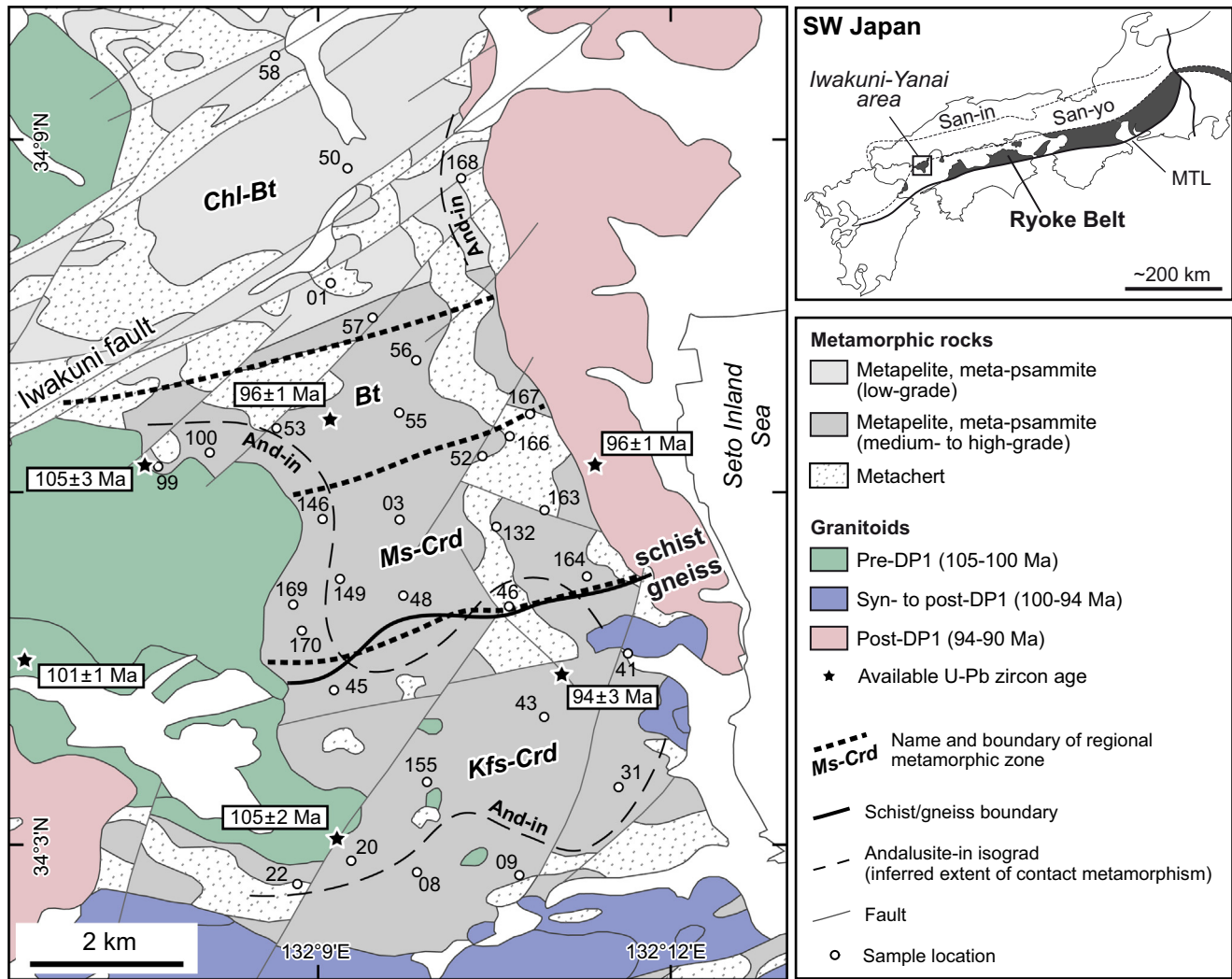
Fig. 1. Geological map of the Ryoke belt in the Iwakuni-Yanai area (SW Japan), with sampling localities. Inset shows the area within the Inner Zone of SW Japan (MTL = Median Tectonic Line). Granitoids are classified according to their emplacement timing relative to the main, regional tectono-metamorphic event (DP1). Available U-Pb zircon ages for granitoids and microgranite dykes (within metasediments) are indicated (Skrzypek et al., 2016). Lithologies are after Sato (1933), Higashimoto et al. (1983) and the Geological Survey of Japan (2012). Metamorphic zone boundaries modified after Ikeda (1993). Schist/gneiss boundary modified after Higashimoto et al. (1983). Mineral abbreviations follow IUGS recommendations after Kretz (1983).
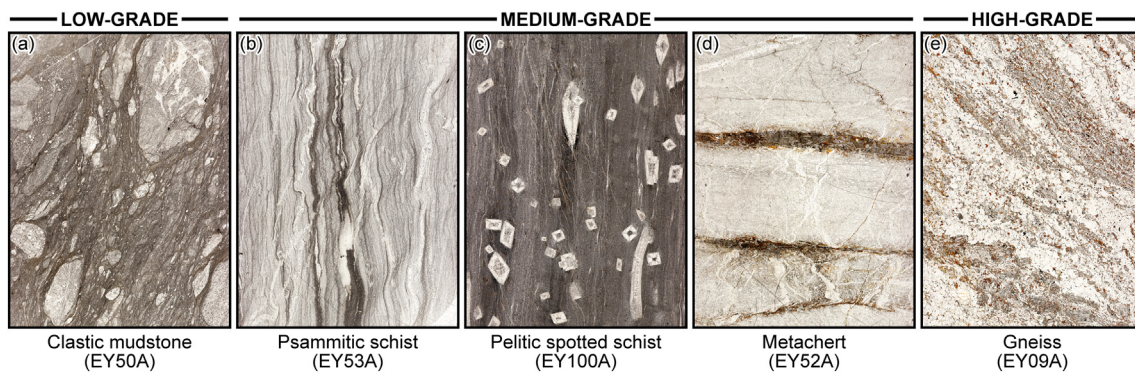

Fig. 2. Scans of thin sections illustrating the different rock types, compositions and textures with increasing metamorphic grade. (a) Low-grade (meta-)mudstone with Qtz-rich clasts and abundant CM in the matrix. (b) Medium-grade psammitic schist with thin, CM-rich pelitic layers. (c) Medium-grade spotted schist with chiastolite porphyroblasts and abundant CM in the matrix. (d) Medium-grade metachert with thin pelitic layers where Ms–Bt laths, yellowish pinitized Crd porphyroblasts and CM are concentrated. (e) High-grade gneiss with alternating Qtz–Pl and Bt–Crd layers, the latter being richer in CM. The terms low-, medium- and high-grade are used in a relative manner. The bottom edge of scans is about 2 cm.

outline (Fig. 3e, f). Such anhedral grains are commonly observed as inclusions in matrix minerals as well as in mica, andalusite or cordierite porphyroblasts. Type III is found in psammitic rocks with intermediate

amounts of CM (8 samples). Type IV corresponds to coarser, stubby or elongated CM grains that mostly accumulate along the boundaries of matrix minerals (Fig. 3g). Backscatter electron images show that the
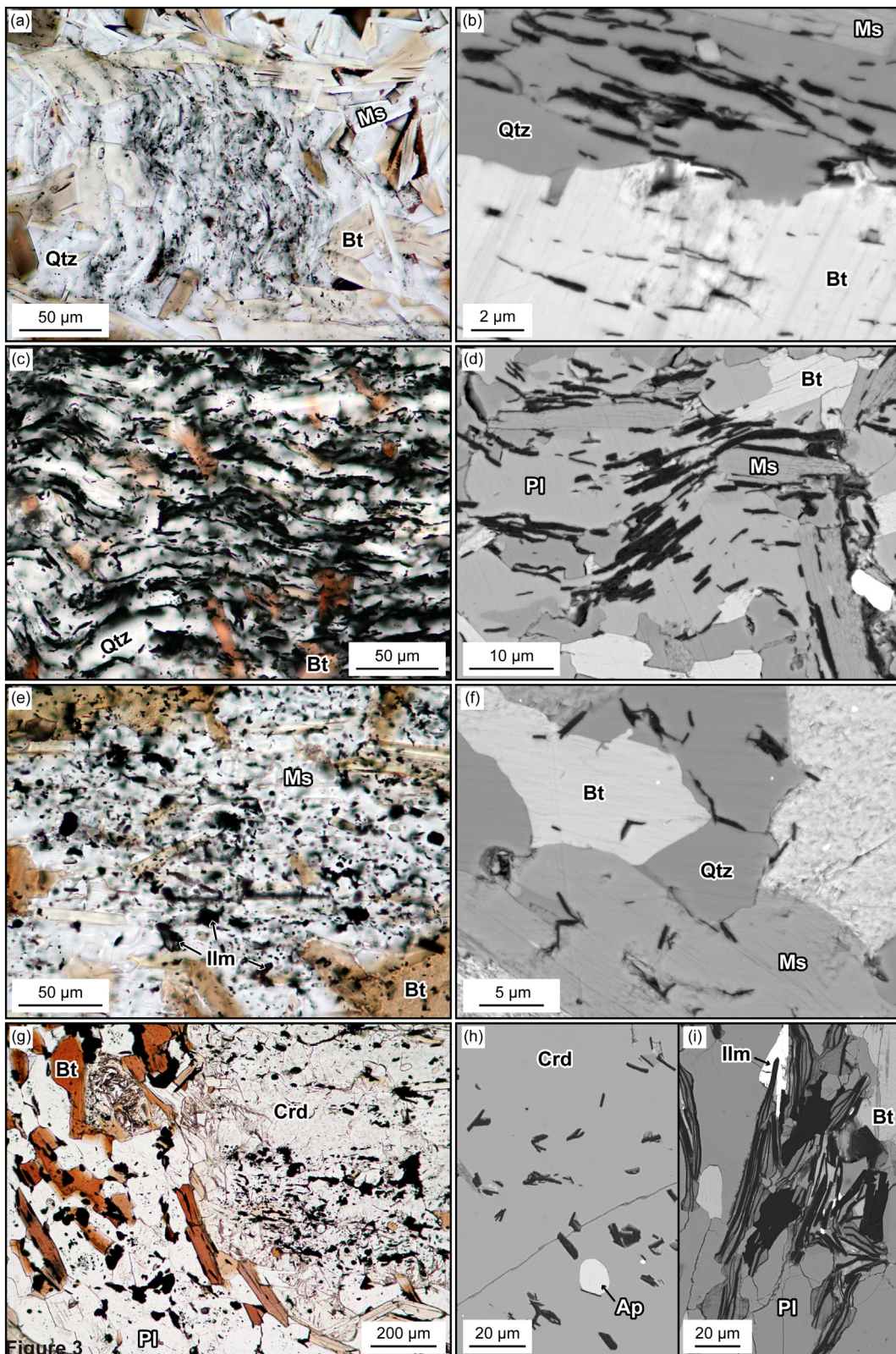
Fig. 3. Photomicrographs (a,c,e,g; plane-polarized light) and backscatter electron images (b,d,f,h,i) illustrating the different textures and morphologies of carbonaceous material. (a,b) Type I (schist sample EY56A) – (a) micro-crenulated, discontinuous trails of tiny CM particles in a Qtz–Ms–Bt matrix; (b) thin oriented CM needles in Bt and Qtz. (c,d) Type II (schist sample EY170A) – (c) weakly folded, nearly continuous layers of elongated CM in the matrix; (d) folded and relatively thick CM laths in a Qtz–Pl–Ms–Bt matrix. (e,f) Type III (metachert sample EY166A) – (e) small and irregular, isolated CM grains in Ms–Bt laths. The larger, rounded opaque minerals are Ilm; (f) thin and short CM laths in micas, Qtz and at grain boundaries. (g,h,i) Type IV (gneiss sample EY09A) – (g) coarse, rounded or irregular CM grains along Pl grain boundaries, next to Bt and inside a Crd porphyroblast. Enlarged views of (h) small CM grains inside Crd and (i) larger CM laths and flakes in the matrix.

matrix CM laths and flakes are markedly larger than CM included in Crd porphyroblasts from the same sample (Fig. 3h, i). Type IV texture is restricted to gneissose rocks from the Kfs — Crd zone (8 samples).

4. The Raman spectrum of carbonaceous material

The Raman spectrum of CM can be divided into a first-order (1000–1700 cm^{-1}) and second-order (2300–3300 cm^{-1}) region (Fig. 4). In the first-order region the only Raman-active band predicted by group theory is the G band at ~1580 cm^{-1} (Fig. 4a), which is ascribed to in-plane atomic displacements (E$_{2g}$ mode, e.g. Dresselhaus et al., 1977; Tuinstra and Koenig, 1970). All other bands arise from the presence of defects such as point defects (vacancies, impurities) or planar defects (crystal edges, stacking faults) that introduce some "disorder" in the lattice and enhance double-resonant Raman scattering (electron-phonon-defect; Thomsen and Reich, 2000). Such bands are therefore named D bands. Because they result from a resonant process these bands are dispersive; their position, shape and intensity vary with the energy of the exciting laser (e.g. Pócsik et al., 1998; Sato et al., 2006; Sinha and Menéndez, 1990; Vidano et al., 1981). For the samples used in this study, only the D1 (~1350 cm^{-1}) and D2 (~1620 cm^{-1}) bands are observed (Fig. 4a). Other authors report the presence of the D″ (~1100 cm^{-1}), D3 (~1500 cm^{-1}) and D4 (~1200 cm^{-1}) bands (see Beyssac and Lazzeri, 2012 for a synthesis of band names).

In the second-order region, overtones or bands due to combination scattering also appear as a result of double-resonant processes (Thomsen and Reich, 2000) and are commonly labeled S (see Henry et al., 2019). The most intense and perhaps most interesting one is the S1 band (also called G' or 2D) at ~2700 cm^{-1} (Fig. 4b). Although its position agrees with S1 being the second harmonic of the D1 band (at 2 x ~ 1350 cm^{-1}), it is even observed in spectra that completely lack the D1 band (Nemanich and Solin, 1979). This is explained by the origin of S1 as a two-phonon resonant band that does not require the presence of defects (electron-two phonons; Reich and Thomsen, 2004). Another consequence of resonant Raman scattering is visible on the S1 band; in mostly two-dimensional (2d) CM the presence of a single electronic band produces only one S1 peak, but the splitting of electronic bands due to interactions between closer graphene layers in three-dimensional (3d) CM causes a splitting of the S1 band (Ferrari et al., 2006; Malard et al., 2009; Fig. 4b) into two peaks at ~2680 cm^{-1} (S1-) and ~ 2720 cm^{-1} (S1+). On the one hand, these positions agree with combinations of the G + D″ and D2 + D″, respectively. On the other hand, Ferrari et al. (2006) showed that the D1 band actually contains two peaks at 1340 and 1360 cm^{-1} whose overtones would precisely be the S1- and S1+ peaks. Two additional bands are observed at ~2450 cm^{-1} (S3) and ~2950 cm^{-1} (S2); they possibly correspond to combinations of the D1 + D″ and G + D1 bands, respectively (Beyssac and Lazzeri, 2012; Fig. 4b).

5. Analytical procedure

All samples were cut perpendicular to the main foliation, and thin sections of 30 μm thickness were prepared and polished with a 3-μm diamond paste before analysis with a Jasco NRS-3100 Raman spetrometer at Kyoto University. The 532 nm (2.33 eV) beam of a diode-pulsed solid-state (DPSS) laser was attenuated (neutral density filtering with optical density = 1) and focused through a 100× objective lens (numerical aperture = 0.95) on the sample (~1 μm beam diameter). The measured laser power on the sample was about 60 μW/m^2 and a degradation of the CM spectrum during laser irradiation was observed in only rare cases. Reflected and transmitted light observations were used to ensure that the analyzed CM was not exposed at the sample surface. A beam splitter mirror directed the scattered light on a Peltier-cooled (−55 °C) CCD detector with 1800 lines/mm grating for a final resolution of about 1 cm^{-1}. Raman shift was calibrated using the 520.7 cm^{-1} band of a silicon wafer. It was cross-checked with the 2840, 2883 and 2905 cm^{-1} bands of polypropylene (Arruebarrena de Báez et al., 1995) before measurements in the second-order region. The spectrometer drift was assessed by measuring the intense emission bands of the built-in Ne lamp before and after each session, and was found to be less than 1 cm^{-1} within a few hours and about 2 cm^{-1} for measurements conducted over an entire day.

The first-order spectrum was measured for the window 760–1780 cm^{-1} and with 4 integrations of 30 s (30–40 spot analyses per sample on different grains). The second-order spectrum was measured for the window 2270–3090 cm^{-1} and with 3 integrations of 15 s (15 spot analyses per sample on different grains). Because changing the center of the measurement window can alter the Raman shift calibration, the first- and second-order spectra were measured during separate sessions and on different grains, but in the same parts of the thin section.

The raw spectra were processed with Fityk 1.3.1 software (Wojdyr, 2010). For first-order data the background was linearly subtracted between 1255 and 1710 cm^{-1} and the visible G, D1 and D2 bands were fitted with Pseudo-Voigt functions based on earlier works (e.g. Beyssac et al., 2003b). The different peak parameters (frequency ω, intensity I, area A, shape s) were exported to calculate mean and standard deviation values for each sample (Table 1, see Supplementary Material for the full dataset). The shape parameter s depicts the relative Gaussian ($s = 0$) and Lorentzian ($s = 1$) contributions in the Pseudo-Voigt function (see Wojdyr, 2010). The G peak has a mean s close to 1 indicating that a Lorentzian fit could be sufficient. Conversely, D1 commonly shows $s = 0.5$, which might reflect the actual presence of two peaks (Ferrari et al., 2006) and accounts for its frequent asymmetrical shape. For second-order data the background was linearly subtracted between 2320 and 3020 cm^{-1} and the visible S1, S2 and S3 bands were fitted with Lorentzian functions (Fig. 4b). Lorentzian functions were chosen to limit the degree of freedom for peak fitting; only ω, I and the half
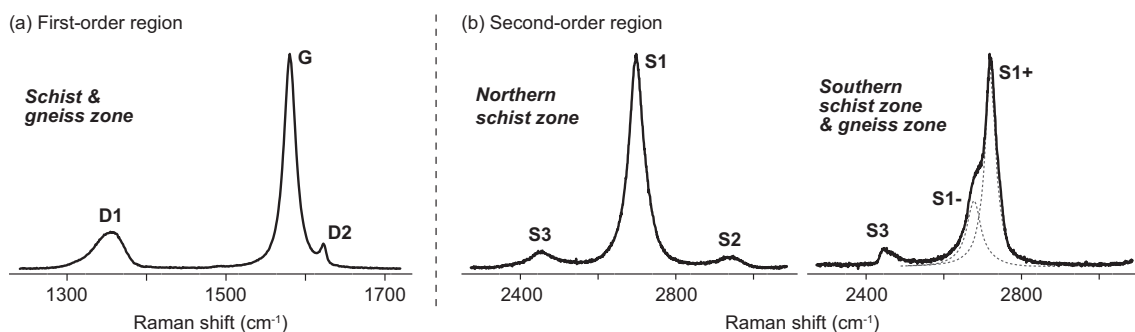
Fig. 4. Typical Raman spectra of CM for the low- to high-grade samples analyzed in the present study. (a) First-order region with the dominant G band and the defect-induced D1 and D2 bands. (b) Second-order region with S1, S2 and S3 bands. The S1 band has a single peak in low-grade samples but splits into two distinct peaks (S1- and S1+) in medium/high-grade ones. Dashed lines show fitting of the split S1 band by two Lorentzian functions.

Table 1
Summary of sample characteristics, CM properties and selected Raman parameters.

Sample	Regional metam. zone	Lithology	Composition	Blasts	N-S distance (m)	Carbonaceous material Abund.	Morph.	Number of analyzed spectra 1st order	no D band	2nd order	single S1	First-order features Ratios R2	±	R1	±	T_CM (°C)	±	Second-order features ΔS1 (cm⁻1)	±	RS1	±
EY58B	Chl-Bt	schist	pelitic		0	++	II	40	—	15	15	0.46	0.04	0.68	0.17	425	19			Single S1 band	
EY50A	Chl-Bt	clastic mudstone	psammitic		1799	+++	II	40	—	15	15	0.35	0.04	0.41	0.08	475	19			Single S1 band	
EY168A	Chl-Bt	spotted schist	pelitic	And	1998	+++	II	40	2	15	—	0.28	0.11	0.20	0.10	515	57	35.7	1.4	0.60	0.12
EY01A	Chl-Bt	metachert	siliceous	(Grt)	3600	++	I	40	—	15	5	0.28	0.08	0.24	0.08	511	41	31.6	2.2	1.06	0.27
EY57A	Chl-Bt	schist	psammitic		4158	+	I	40	—	15	3	0.28	0.05	0.21	0.08	514	27	33.2	1.6	0.78	0.11
EY56A	Bt	schist	pelitic		4844	++	I	40	—	15	—	0.25	0.07	0.21	0.08	526	40	34.0	1.1	0.72	0.12
EY55A	Bt	schist	pelitic		5663	+++	I	40	—	15	—	0.29	0.06	0.22	0.07	508	29	36.1	1.7	0.66	0.10
EY167A	Ms-Crd	schist	pelitic		5730	+++	II	40	—	15	—	0.15	0.08	0.10	0.06	583	43	36.9	1.7	0.59	0.14
EY53A	Bt	schist	siliceous	(Grt)	5862	++	II	40	—	15	—	0.29	0.05	0.23	0.06	508	24	33.3	0.8	0.92	0.14
■ Low								20	—	5	—	0.33	0.03	0.28	0.06	488	13	33.0	0.9	1.10	0.06
■ High								20	—	10	—	0.25	0.02	0.18	0.02	528	11	33.4	0.8	0.83	0.04
EY166A	Ms-Crd	metachert	siliceous	Ms	6073	+	III	40	—	15	—	0.20	0.08	0.13	0.07	556	41	36.9	1.7	0.53	0.14
EY100A	Bt	spotted schist	pelitic	And	6221	+++	III	40	—	15	—	0.23	0.08	0.16	0.08	537	46	36.6	1.3	0.57	0.10
EY52A	Ms-Crd	metachert	siliceous	Ms, Crd	6376	+	III	40	—	15	—	0.23	0.08	0.16	0.07	538	41	36.2	1.5	0.58	0.10
EY99BI	Bt	spotted schist	pelitic	And, Crd	6422	+++	II	40	—	15	—	0.13	0.07	0.07	0.05	597	39	37.8	1.1	0.50	0.08
EY163A	Ms-Crd	spotted schist	psammitic	Crd	7249	+	III	40	—	15	—	0.16	0.08	0.11	0.07	577	46	36.3	1.0	0.55	0.09
EY146A	Ms-Crd	spotted schist	psammitic	And	7307	++	II	40	—	15	—	0.20	0.10	0.14	0.09	554	54	36.6	1.4	0.52	0.07
EY03A	Ms-Crd	metachert	siliceous	Ms, Crd	7345	+	I	40	—	15	—	0.30	0.08	0.24	0.09	503	41	36.4	1.1	0.69	0.07
EY132A	Ms-Crd	spotted schist	psammitic	Crd	7492	+	II	40	—	15	—	0.16	0.08	0.10	0.06	580	43	36.1	1.6	0.59	0.11
■ Low								20	—	6	—	0.22	0.04	0.15	0.04	543	22	34.7	0.9	0.71	0.06
■ High								20	—	9	—	0.09	0.04	0.05	0.03	616	24	37.0	1.4	0.52	0.05
EY149A	Ms-Crd	schist	psammitic	Crd	8257	++	III	40	—	15	—	0.20	0.08	0.13	0.07	556	46	36.5	2.1	0.61	0.14
■ Low								27	—	5	—	0.25	0.05	0.18	0.05	529	26	34.2	0.5	0.79	0.07
■ High								13	—	10	—	0.10	0.04	0.05	0.02	611	21	37.6	1.6	0.52	0.06
EY164A	Ms-Crd	schist	pelitic		8307	+++	II	40	—	15	—	0.21	0.08	0.15	0.08	548	46	35.5	1.2	0.66	0.10
EY48A	Ms-Crd	schist	psammitic		8543	++	III	40	—	15	1	0.24	0.07	0.17	0.07	535	40	36.3	2.0	0.64	0.13
EY169A	Ms-Crd	schist	psammitic	Bt	8643	++	II	40	—	15	—	0.17	0.07	0.11	0.06	572	42	36.2	1.6	0.67	0.17
EY46B	Ms-Crd	hornfels	pelitic	And, Crd	8750	+	III	40	—	15	—	0.15	0.06	0.08	0.05	583	37	38.5	1.8	0.50	0.11
EY170A	Ms-Crd	schist	pelitic	Bt	9057	+++	II	40	—	15	—	0.24	0.10	0.19	0.11	534	55	36.3	1.5	0.63	0.15
EY41B	Kfs-Crd	gneiss	psammitic		9533	+	IV	40	14	15	—	0.09	0.11	0.08	0.23	619	61	40.8	2.5	0.40	0.12
EY45B	Kfs-Crd	gneiss	psammitic		10,002	+	III	40	—	15	—	0.13	0.08	0.07	0.06	595	44	38.5	1.6	0.47	0.08
EY43B	Kfs-Crd	gneiss	psammitic	And, Crd	10,500	++	IV	40	22	15	—	0.05	0.07	0.03	0.04	643	41	40.8	1.5	0.39	0.07
EY155A	Kfs-Crd	gneiss	pelitic		11,481	+	IV	30	14	15	—	0.06	0.08	0.03	0.04	639	46	40.7	1.8	0.37	0.10
YN31A	Kfs-Crd	gneiss	psammitic		11,631	++	IV	40	21	15	—	0.07	0.12	0.05	0.12	631	65	41.7	1.4	0.34	0.06
EY20A	Kfs-Crd	gneiss	psammitic		12,694	++	IV	30	19	15	—	0.02	0.05	0.01	0.02	659	27	41.2	1.6	0.35	0.05
EY08C	Kfs-Crd	gneiss	psammitic		12,897	++	IV	30	17	15	—	0.04	0.07	0.02	0.05	648	43	42.3	1.1	0.32	0.03
EY09A	Kfs-Crd	gneiss	psammitic	Crd	12,981	++	IV	40	31	15	—	0.03	0.06	0.01	0.03	655	37	41.8	1.6	0.36	0.04
EY22A	Kfs-Crd	meta-chert	siliceous		13,039	+	IV	30	19	15	—	0.07	0.12	0.04	0.10	631	67	42.2	1.1	0.32	0.03

Abund. = relative CM abundance in thin section; Morph. = morphological type of CM.
T_CM calculated from R2 ratios with the calibration of Aoya et al. (2010) for a 532 nm laser.
Results for low- and high-grade (Low/High) subgroups of analyses are shown for indication.

width at half maximum can be varied in this case, whereas the additional *s* parameter is available for a Pseudo-Voigt function. This was chosen in agreement with previous works (e.g. Cançado et al., 2008) and because the main objective was to measure the splitting of S1 without the possible influence of differing shapes for the S1+ and S1- peaks.

The main Raman parameters that will be discussed are defined as follows: R1, dimensionless intensity ratio = $[I_{D1}/I_G]$; R2, dimensionless area ratio = $[A_{D1}/(A_{D1} + A_{D2} + A_G)]$; ΔS1, absolute frequency difference in cm^{-1} = $[|\omega_{S1+} - \omega_{S1-}|]$; RS1, dimensionless intensity ratio = $[I_{S1-}/I_{S1+}]$. Temperatures (T$_{CM}$) were calculated using R2 ratios and the relationship derived for contact metamorphism by Aoya et al. (2010) because it is the only calibration available for a 532 nm excitation wavelength. Its quadratic equation gives temperatures that are 10 °C lower (at low-grade) but up to 28 °C higher (at high-grade) than those obtained with the calibration of Beyssac et al. (2002a).

6. Results

6.1. First- and second-order regions of the Raman spectrum

The intense G band dominates the first-order spectrum of CM in all samples (Fig. 5a). It is accompanied by the D1 and D2 bands whose intensities decrease from north to south while G becomes narrower. The D1 band evolves from a symmetrical peak slightly higher than half of the G band to a smaller asymmetrical peak, and eventually disappears (Fig. 5a). The narrow and less intense D2 band clearly appears on the high frequency shoulder of the G band in low-grade samples but vanishes in high-grade ones (Fig. 5a). In high-grade samples the proportion of spectra without any "disorder" band ranges from 35 to 78% of all analyzed spectra (Table 1). The R1 and R2 ratios are uncorrelated with the pelitic, psammitic or siliceous composition of the samples (Table 1). They are partly linked with CM texture as low ratios are generally obtained from type IV CM, which is only found in high-grade gneiss samples.

The second-order spectrum is dominated by the S1 band, with the less intense S2 and S3 bands appearing on each side of it (Fig. 5b). The two northernmost samples (EY58B, EY50A) exhibit a single S1 band centered at ~2700 cm^{-1}. In all other samples S1 splits into the S1- and S1+ peaks whose frequency difference ΔS1 increases from north to south (Fig. 5b). Two low-grade (EY01A, EY57A) and one medium-grade (EY48A) sample preserve mixed results with a larger proportion of spectra showing the double S1 band and a few having a single S1 band (Table 1). The broad and low-intensity S2 band tends to shrink with rising metamorphic grade but does not entirely disappear in high-grade samples. The intensity of the weak S3 band does not significantly change with increasing metamorphic grade, but its shape becomes more asymmetrical (Fig. 5b). Like the R1 and R2 ratios, the RS1 and ΔS1 parameters do not show any correlation with pelitic, psammitic or siliceous sample compositions; they are partly linked with CM texture in the case of type IV CM from high-grade gneiss (Table 1).

6.2. Intra-sample variation of Raman parameters

The variability of Raman parameters in each sample was assessed using the R2 and RS1 ratios (see Supplementary Material). In all samples the mean of R2 data converges towards a constant value for more than 20–30 analyses while that of RS1 becomes nearly constant above ~10 analyses. In high-grade samples, where first-order spectra devoid of "disorder" bands are common, a total of 30 analyses was sufficient to reach a constant mean for R2. The acquisition of 30-40 first-order and 15 second-order spectra was therefore sufficient to confidently characterize R2 and RS1 in a sample. This difference in the number of first- and second-order spectra that needed to be acquired is mostly explained by larger intra-sample variations in the area of the D1 band.

Figure 5
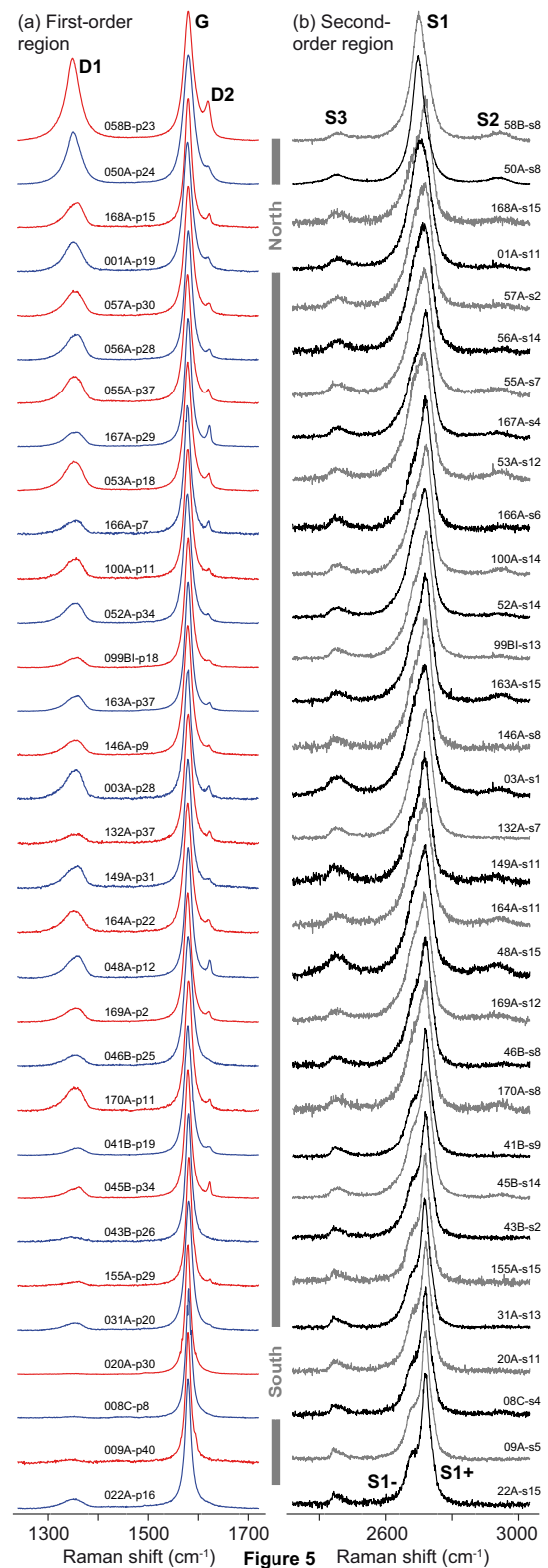
Fig. 5. Representative first- and second-order Raman spectra of CM for all samples, sorted from north to south (spot names indicated). (a) First-order region with defect-induced bands decreasing and eventually disappearing towards the south. (b) Second-order region with the transition from single S1 to double S1- and S1+. Vertical intensity scale is arbitrary. Raw spectra are trimmed to show only the relevant regions.

Histograms of R2 and RS1 distribution were also inspected to detect the presence of multiple CM populations. For most samples the distribution of R2 and RS1 defines a single maximum, and the mean of R2 or RS1
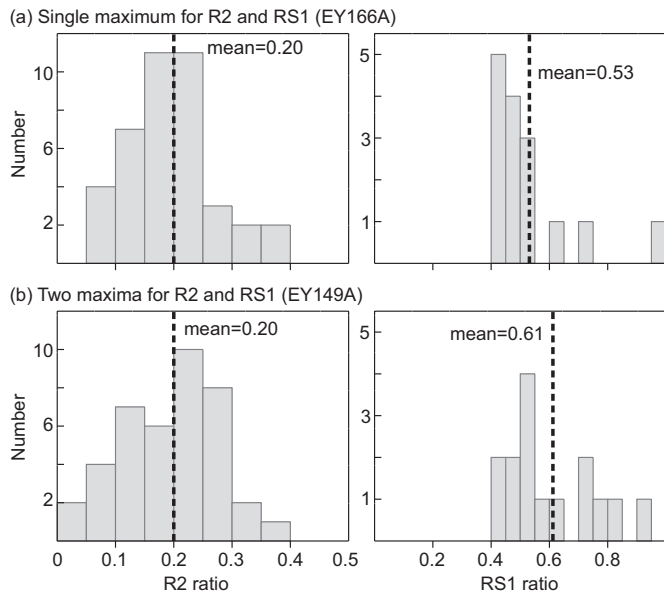
Fig. 6. Histograms of R2 ($n = 40$) and RS1 ($n = 15$) distribution in two samples with similar mean R2 values (0.20) to illustrate differences in the variability of first- and second-order Raman parameters. (a) Sample EY166A with a single maximum for both R2 and RS1 distributions. Each mean value matches the maximum of the distribution. (b) Sample EY149A with a slightly bimodal distribution of both R2 and RS1. Although a low- and high-grade group can be distinguished, the final dataset uses the mean of all analyses (see text and Table 1).

coincides with the maximum of its frequency distribution (Fig. 6a). Samples for which a contact metamorphic overprint is inferred (i.e. with porphyroblasts) tend to show broader R2 distributions but preserve only one CM population. For three samples (EY53A, EY132A, EY149A), however, a bimodal distribution of both R2 and RS1, and the observation that mean R2 and RS1 values rather lie in between two maxima may suggest the presence of two CM populations (Fig. 6b). In these samples a low- and high-grade group can be distinguished, but no correlation with the shape or location (e.g. matrix vs. inclusions in porphyroblasts) of CM grains is apparent. The difference between both groups is also not as extreme as in cases where mixing of metamorphic and detrital CM is inferred (e.g. Kouketsu et al., 2019). In order to describe the spatial variation of Raman parameters, such subpopulations are therefore ignored and a mean value for the whole sample is used (Table 1).

6.3. Spatial variation of Raman parameters

In first-order spectra the intensity of the D1 and D2 bands decreases from north to south (Fig. 5a). This translates into a decrease of both R1 (0.68 to 0.01) and R2 (0.46 to 0.02) ratios and a concomitant increase in calculated temperature T_{CM} (425 to 659 °C) along the exposed metamorphic gradient (Fig. 7a,b, Table 1). In the Bt and Ms–Crd zones T_{CM} also increases towards the west and east as samples approach the surrounding granites (Fig. 8a). It is depicted by a large scatter of R1 (0.07–0.24) and R2 values (0.13–0.30) in this segment of the N-S transect (Fig. 7a, b). In map view the variation of T_{CM} defines a relatively low-T domain ($T_{CM} < 535$ °C) to the north of the Iwakuni fault. This domain narrows to the south of the Iwakuni fault but persists up to the schist/gneiss boundary in the axial part of the metasedimentary belt (Fig. 8a). It is surrounded by a medium-T domain ($535 < T_{CM} < 600$ °C) close to the granitoids and the schist/gneiss boundary while a high-T
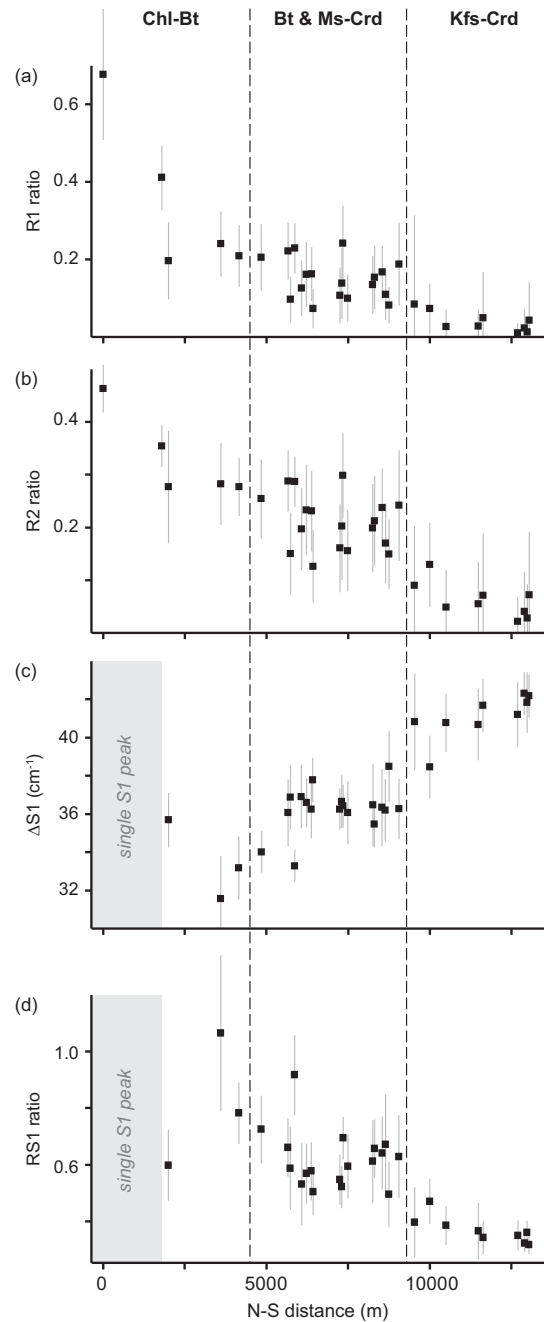

Fig. 7. Evolution of selected first- and second-order Raman parameters from north to south. (a-b) Gradual decrease of the first-order R1 and R2 ratios. (c-d) Stepwise variation of the second-order ΔS1 and RS1 parameters (calculated for a split S1 band). The error bar reflects the standard deviation of all measurements in a sample. The boundaries of metamorphic zones are indicated.

domain ($T_{CM} > 600$ °C) occurs in gneissose rocks from the Kfs–Crd zone (Fig. 8a).

The major change in the second-order spectra is related to the splitting of the S1 band. The two northernmost samples exhibit a single S1 band, whereas all other samples show mostly or exclusively the two S1- and S1+ peaks (Fig. 5b). From north to south the intensity of S1+ increases with respect to that of S1- (RS1 = 1.06 to 0.32) and the spacing ΔS1 between these peaks increases (31.6 to 42.3 cm^{-1}) in a rather stepwise manner (Fig. 7c,d). In map view the variation of ΔS1 defines three domains delimited by NE–SW- to E–W-trending boundaries; no
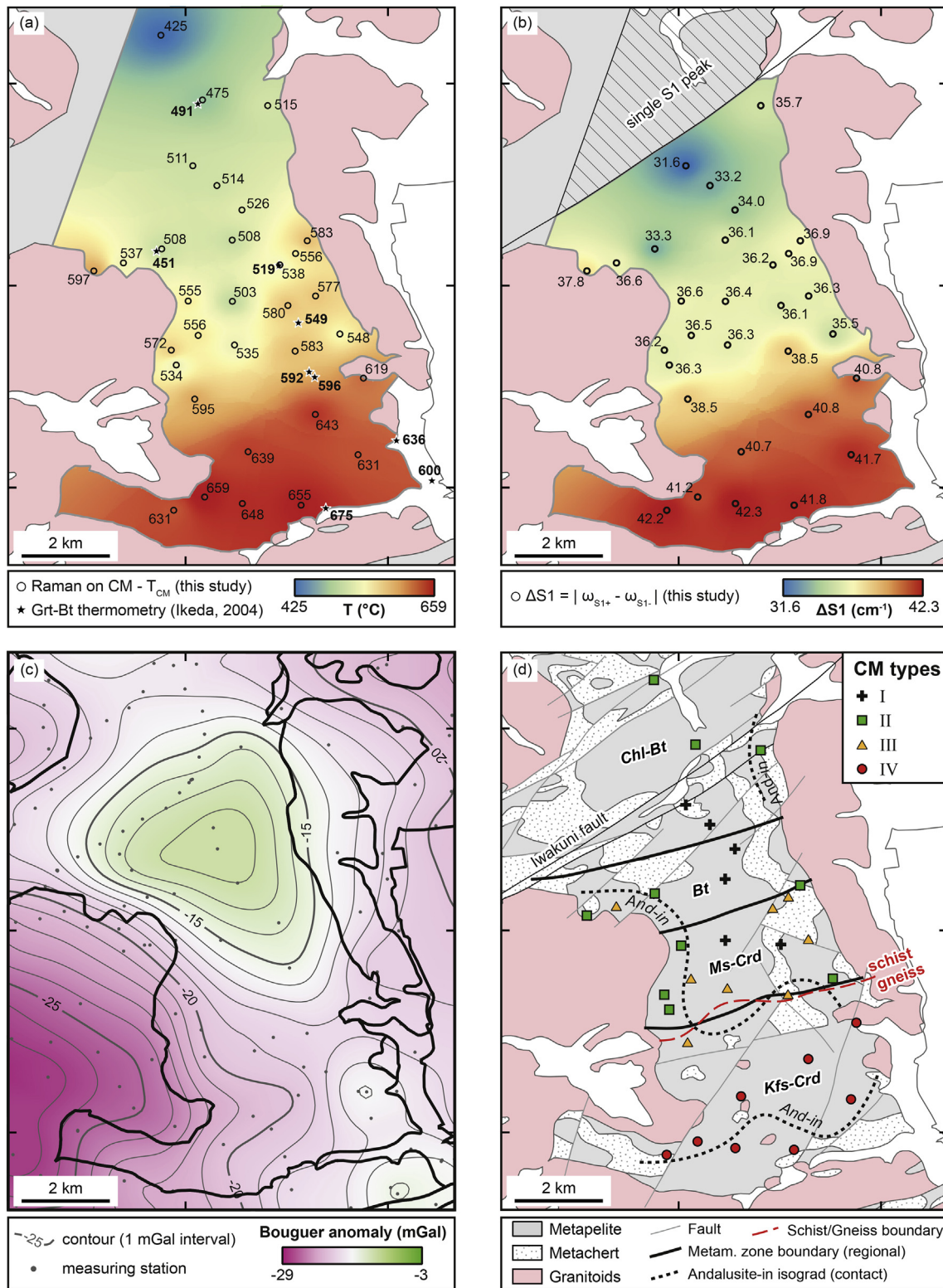
Fig. 8. Spatial distribution of selected Raman parameters, and comparison with gravity anomaly data and the metamorphic structure of the Iwakuni-Yanai area. (a) Map distribution of T_{CM} calculated with the R2 ratio. Black stars and bold numbers show the results of Grt–Bt thermometry (Ikeda, 2004) for comparison. (b) Map distribution of $\Delta S1$ ($\Delta S1 = 0$ north of the Iwakuni fault). (c) Bouguer anomaly map (2.67 g/cm^3 terrain correction) for the extent of the study area (Geological Survey of Japan, 2013; Komazawa, 2013, and references therein). (d) Lithological map with the main features generated by contact (And-in isograd) and regional (mineral zones) metamorphism (Higashimoto et al., 1983; Ikeda, 1998; Skrzypek et al., 2016), and with the distribution of CM textural types. The interpolated maps for T_{CM} and $\Delta S1$ were calculated with the same parameters (see Appendix).

splitting of the S1 band is observed to the north of the Iwakuni fault, a domain of lower $\Delta S1$ (32–38 cm^{-1}) broadly coincides with the schist zone and one of higher $\Delta S1$ (>38 cm^{-1}) with the gneiss zone

(Fig. 8b). Parameters calculated for the S2 and S3 bands do not show any clear trend, except for the full width at half maximum of S3 that slightly decreases (~ 60 to 40 cm^{-1}) from north to south.

7. Geological significance of RSCM data

7.1. Interpretation of results from first-order Raman spectra

7.1.1. Pre-DP1 contact metamorphism

A domain of medium T_{CM} values (535–600 °C) is imaged along the western granitoid that intrudes the schist zone (Fig. 8a). This domain closely follows the contact aureole defined by the occurrence of pre-DP1 andalusite porphyroblasts (Skrzypek et al., 2016; Fig. 8d). This temperature range is typical for andalusite appearance in pelitic lithologies affected by contact metamorphism (e.g. Pattison and Tracy, 1991) and indicates that RSCM confidently reveals the thermal effect of pre-DP1 contact metamorphism, as already shown by several studies of metamorphic aureoles (e.g. Aoya et al., 2010; Nakamura and Akai, 2013). The narrow width of the thermal aureole (< 1 km), despite a subhorizontal contact with metasediments, additionally points to a relatively low host-rock temperature at the time of intrusion.

A prolongation of the aureole in the gneiss zone was proposed based on the presence of the western granitoids at shallow depth beneath metasedimentary rocks, although the pre-DP1 origin of andalusite blasts is hard to establish there (Skrzypek et al., 2016; Fig. 1). It can be supported by the gravity anomaly map (Komazawa, 2013, and references therein) that correlates well with the inferred extent of the entire aureole (Fig. 8c, d). The values for T_{CM} in the gneiss zone (> 600 °C) are, however, markedly higher than in the north and seem to result from the subsequent regional overprint. An argument for the regional origin of these high T_{CM} is the dominant occurrence of coarser-grained type IV CM in the gneiss zone (Fig. 8d), whereas this type is never observed in the north, even in a sample located at the contact with a granite where T_{CM} reaches 597 °C (EY99BI; Table 1). This suggests that a different heating event was necessary to generate the CM texture and crystallinity observed in the gneiss zone.

7.1.2. Syn-DP1 regional metamorphism

Apart from peripheral domains of the schist zone where T_{CM} exceeds ~535 °C, the axial part of the belt shows T_{CM} increasing from ~425 to 535 °C (Fig. 8a). Following a gap at the schist/gneiss transition, the gneiss zone exhibits homogeneously higher T_{CM} values of ~600–660 °C associated with coarser-grained type IV CM (Fig. 8a). The entire succession agrees with the Grt-Bt thermometry results of Ikeda (2004) for samples located away from the influence of granitoids (compare results on Fig. 8a); combined temperature estimates indicate 450–500 °C for the Chl — Bt zone, 500–525 °C for the Bt zone, 500–535 °C for the Ms. — Crd zone and 600–660 °C for the Kfs — Crd zone (Ikeda, 2004; Table 1). Both RSCM and Grt-Bt thermometry therefore constrain the well-known N-S regional metamorphic gradient that has also been described in other parts of the Ryoke belt (e.g. Hokada, 1998; Kawakami, 2001; Miyazaki, 2010).

7.1.3. Post-DP1 contact metamorphism

The eastern granite intrudes only the schist zone and its boundary with metasedimentary rocks is subvertical. Its contact aureole is not easily mapped due to the presence of abundant siliceous lithologies and is only traced in the north (Fig. 8d). The spatial distribution of T_{CM} nevertheless reveals a wide domain of medium temperatures (540–580 °C) along the southern border of the granite (Fig. 8a). A post-DP1 contact metamorphic origin is inferred for this domain, as its outline does not follow the regional metamorphic zones, and because a limited extension of the eastern granite towards the SW is consistent with gravity anomaly data (Fig. 8a,c). Regardless of the intrusion that caused the temperature increase, this case demonstrates the usefulness of RSCM data for identifying thermal overprints in petrologically "inappropriate" lithologies and for tracing the extent of buried magmatic bodies. These aspects have already been emphasized with XRD (e.g. Tsuchiya et al., 1987) as well as RSCM (e.g. Hilchie and Jamieson, 2014) data. If the heating event occurred after regional metamorphism,

the possibility for delayed CM recrystallization (Beyssac et al., 2019) must be discussed. This is done in Section 8 with the help of both first- and second-order Raman data.

7.2. Interpretation of results from second-order Raman spectra

Unlike for T_{CM}, the evolution of the S1 band defines three domains separated by E — W trending boundaries. A single S1 peak north of the Iwakuni fault zone is followed by a weak to mostly moderate ΔS1 in the schist zone and a higher ΔS1 in the gneiss zone (Fig. 8b). This pattern is parallel to the E — W trending metamorphic zones produced by the regional overprint, whereas an increase in ΔS1 towards the surrounding granitoids is not evident (Fig. 8b). It strongly suggests that the second-order S1 band records the effect(s) of the regional tectono-metamorphic event DP1.

The transition from a single to double S1 band occurs across the Iwakuni fault zone (Fig. 8b). For XRD data available along the same transect, a sharp decrease in the full width at half maximum (β) of the (002) peak in CM from 0.40–0.83° to less than 0.36° is reported across the fault (Ikeda, 1992). Grew (1974) and Itaya (1981) document the same drastic drop in β when the C content of CM increases above 90–97%, in agreement with the commonly observed decrease of H — N — O — S in CM with metamorphic grade (Izawa, 1968; Wada et al., 1994). It therefore appears that the expulsion of non-C elements, some of them being known to impede graphitization (e.g. Franklin, 1951), is responsible for the splitting of the S1 band.

The splitting of the second-order S1 band is explained by the electronic band structure of CM; a single S1 peak reflects the absence of electronic interaction between graphene layers, whereas a double S1 peak points to interlayer interaction as the graphene planes become closer to each other and acquire regular ABAB stacking (e.g. Ferrari et al., 2006). The mineralogical significance is that 2d CM acquired a 3d structure south of the Iwakuni fault. Increasing ΔS1 values towards the south indicate that the 3d structure still evolved, i.e. that both interlayer spacing (d_{002}) decreased and out-of-plane ordering increased to a maximum value of 42.3 cm^{-1} (sample EY08C). For comparison, the average d_{002} in the Kfs — Crd zone is 3.358 Å (Ikeda, 1992) while Lespade et al. (1984) report maximum values of ΔS1 ≈ 45 cm^{-1} and d_{002} ≈ 3.355 Å for heat-treated graphitizing carbon (d_{002} = 3.3539 Å for ideal graphite; Kwiecińska and Petersen, 2004).

8. General implications for RSCM

8.1. S1 band splitting and the 500 °C isotherm

In the study area, the splitting of S1 occurs together with a hardly detectable lithological transition from weakly-metamorphosed sediment to schist (Higashimoto et al., 1983), for T_{CM} between 475 and 511 °C (Fig. 8a), and across a pressure change from 0.8 to 1.9 kbar (difference between the Chl — Bt and Ms. — Crd zones; Kouketsu et al., 2014b). The splitting of S1 is consistently observed above 2200 °C in heat-treated industrial graphite (Bernard et al., 2010; Pimenta et al., 2007; Wilhelm et al., 1998), but a higher pressure and longer heating duration are also able to shift the S1 band to a higher frequency in experiments conducted at 1000 °C (Beyssac et al., 2003a). For metapelites from different metamorphic belts Wopenka and Pasteris (1993) report a shift of the S1 band above chlorite grade, i.e. for P — T conditions higher than 500 °C/4 kbar (Pasteris and Wopenka, 1991). Using an extensive sample set Beyssac et al. (2002a) observe the splitting of S1 above ~500 °C without any apparent link with pressure. In the Gyoja-yama contact metamorphic aureole (Japan), Nakamura and Akai (2013) show that the S1 band splits between 510 and 530 °C. The change from a single to a double S1 band was also recognized between 495 and 500 °C in the Nelson aureole, Canada (Beyssac et al., 2019).

The review of data highlights that the splitting of S1 always occurs at about 500 °C regardless of lithology, pressure or tectonic setting.

Accordingly, temperature is considered to be the major factor influencing the splitting of S1, hence the appearance of 3d CM in metamorphic rocks. Nakamura (1995) also recognized that a β value of 0.3° was consistently attained at 500 °C in both regional and contact metamorphic settings. The present study therefore emphasizes that a simple, visual comparison of second-order spectra is a powerful approach to locate the 500 °C isotherm in metamorphic terrains and to approximately distinguish between H–N–O–S-bearing and C-richer carbonaceous material.

8.2. Applicability of RSCM thermometry: Delayed CM recrystallization or not?

Along the SW margin of the eastern granite a medium-temperature domain is ascribed to post-DP1 contact metamorphism (Fig. 8b). This interpretation requires explaining why no delayed CM recrystallization is observed as in Beyssac et al. (2019). A first possibility is that the heating event was not younger than regional metamorphism. However, the occurrence of 96–94 Ma-old microgranite dykes up to the centre of the metasedimentary belt (Fig. 1) and the gravity anomaly map (Fig. 8c) support a small extension of the eastern granite at depth, and back the post-DP1 origin of the thermal overprint. A second possibility is that the presence/absence of delayed recrystallization depends on the crystallinity of the CM precursor.

Observations from the present study rather agree with those of Delchini et al. (2016) who showed that samples regionally metamorphosed at ~560 °C were still able to record T_{CM} of 616–628 °C due to subsequent contact metamorphism (their samples J2a and J2.5a). The only place where T_{CM} is somewhat lower than expected lies at the northern margin of the eastern granite. There, sample EY168A records T_{CM} = 515 °C although the presence of andalusite blasts could hint at a slightly higher temperature, like in the western aureole (Fig. 8a). Beyssac et al. (2019) estimate pre-intrusion regional temperatures of ~500 °C in the Ballachulish Complex, i.e. conditions at which CM is still far from ideal graphite. A similar difference exists between the northern and southern margins of the eastern granite; ΔS1 in the northern Chl–Bt zone is low (< 36 cm^{-1}) and points to limited 3d ordering, whereas constant and higher ΔS1 values in the Bt and Ms–Crd zones indicate increased 3d ordering, likely acquired during regional metamorphism (Fig. 7c).

In the light of available data, it therefore appears that CM recrystallization during a subsequent thermal overprint is, at least in part, controlled by the 3d structure of the CM precursor. Should 3d CM, yet with still low out-of-plane ordering (ΔS1 < 36 cm^{-1}), be thermally overprinted then could the elimination of in-plane defects remain sluggish and lead to a discrepancy with other thermometric estimates (e.g. Beyssac et al., 2019). Conversely, thermal overprinting of CM with better 3d ordering (ΔS1 ≥ 36 cm^{-1}) would more efficiently remove in-plane defects and provide reliable RSCM temperature estimates (e.g. Delchini et al., 2016; this study). It is similarly expected from transmission electron microscope observations that in-plane crystallite growth can further proceed once stacked graphene layers have reached a sufficient degree of out-of-plane ordering (e.g. Rouzaud et al., 1983).

8.3. Discrepancy between first- and second-order Raman data

A key result of the study is the partial discrepancy between first- and second-order Raman data, namely R2 and ΔS1 (Fig. 9). The distribution of R2 and associated T_{CM} partly matches the extent of contact metamorphic aureoles, whereas that of ΔS1 follows the regional metamorphic zones (Fig. 8a,b). The question is whether ΔS1 values are lower or higher than expected for a local T_{CM}.

From the Iwakuni fault to the schist/gneiss boundary, a north-south profile in the axial part of the belt reveals increasing ΔS1 from ~33 to above 36 cm^{-1}, whereas T_{CM} remains nearly constant at ~510 °C (Fig. 8a,b). Conversely, a west-east profile in the Bt and Ms–Crd zones shows that ΔS1 stays constant (~ 36 cm^{-1}) while T_{CM} increases from
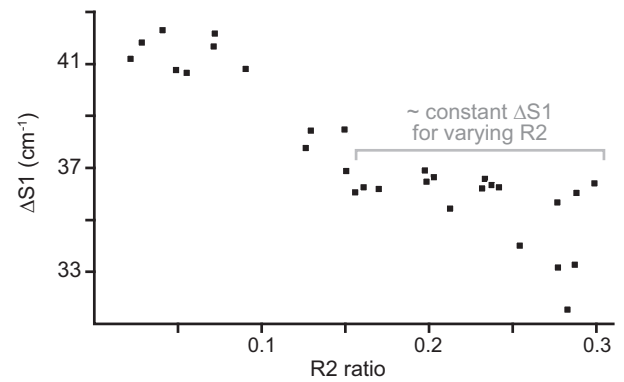

Fig. 9. Plot of ΔS1 vs. R2 for samples south of the Iwakuni fault, i.e. with a split S1 band (n = 30). Note the spread of R2 values for samples having a nearly constant ΔS1 of ~36 cm^{-1}.

~500 to 600 °C towards the surrounding granitoids (Fig. 7b,c). This indicates that ΔS1 is higher than expected for the T_{CM} values obtained in the axial part of the belt, where the influence of contact metamorphism is thought to be weaker. A similar behaviour is observed with the XRD data of Ikeda (1992); from north to south the out-of-plane crystallite size L_c increases throughout the Chl–Bt zone (~100 to 230 Å) but clusters at a constant value in the Bt and Ms–Crd zones (~280 Å; Fig. 10a). A west-east profile across the Bt and Ms–Crd zones reveals uniform L_c values despite varying T_{CM}, with a noticeable L_c increase only close to the eastern granite (Fig. 10b).

All observations call for a process that could generate homogeneous ΔS1 and L_c values without a proportional impact on R2 and T_{CM}. The ΔS1 parameter relates to the *out-of-plane* structure of CM (e.g. Beyssac and Lazzeri, 2012; Cançado et al., 2008; Ferrari et al., 2006), and Lespade et al. (1984) found a correlation between increasing ΔS1 and decreasing interlayer spacing d_{002}. Similarly, the out-of-plane length of coherent crystallites L_c is calculated using the XRD value of β, which can be regarded as a measure of out-of-plane distortion of the graphene layers (Fischbach, 1970). Conversely, R2 involves the area of "disorder" bands in the first-order Raman spectrum, which arises from the presence of *in-plane* defects in CM (e.g. Ferrari and Robertson, 2000). The intensity of defect-induced bands was also shown to decrease with increasing in-plane crystallite size L_a (e.g. Knight and White, 1989; Tuinstra and Koenig, 1970). In order words, factors that can lead to homogeneous out-of-plane ordering despite variable in-plane crystallinity must be sought.

8.3.1. Nature of CM precursor
Numerous works have emphasized that the degree of graphitization depends on the nature of the CM precursor (e.g. Franklin, 1951; Inagaki, 1996; Rouzaud and Oberlin, 1989). For example, heat treatment of deposited carbon films results in faster and more complete graphitization for thick films compared to thin ones (Rouzaud et al., 1983). Different CM textures are recognized in the area, with relatively thin CM type I being found in the axial part of the belt and thicker type II occurring next to granitoids (Figs. 3a-d, 8d). This difference likely arises from pre-D1 contact metamorphism and could have led to contrasted graphitization during subsequent tectono-thermal events, but it cannot account for the uniform ΔS1 and L_c values observed in the Bt and Ms–Crd zones.

8.3.2. Fluids
Fluids are invoked to explain the presence of CM with unusually low or high crystallinity in metamorphic rock samples. On the one hand, variable or unexpectedly low CM crystallinities were partly attributed to the presence of fluid with high methane (Wintsch et al., 1981) or low oxygen (Large et al., 1994) fugacity, which limited the graphitization process. On the other hand, CM grains found in greenschist facies rocks but indicating higher temperatures were explained by the

(a) XRD data – N-S profile (Ikeda, 1992)

(b) XRD and Raman data, Bt & Ms-Crd zones – W-E profile
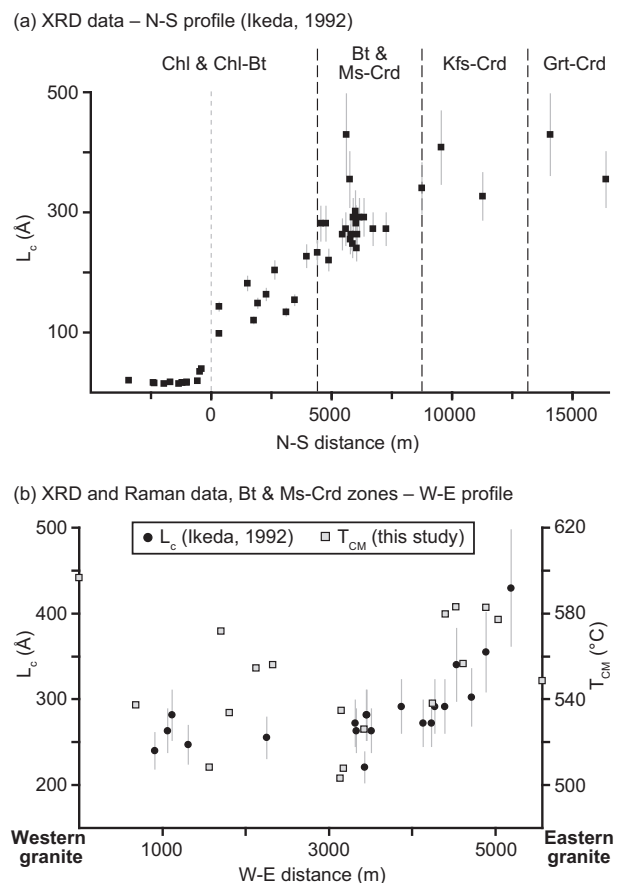
Fig. 10. Evolution of XRD and Raman data along N-S and W-E profiles. (a) N-S variation of crystallite thickness L_c (Ikeda, 1992). The error bars reflect the 0.03° standard deviation ascribed to β by Ikeda (1992) and propagated in the calculation of L_c. Note that the extent of the profile is larger than for the present Raman dataset. (b) Comparison of L_c (Ikeda, 1992) and T_{CM} (this study) data for the Bt and Ms–Crd zones, as a function of W-E position.

precipitation of higher-crystallinity (lower R2) CM from hydrothermal fluids (Kříbek et al., 2008). The circulation of C-bearing fluid is particularly well evidenced by the pervasive network of quartz veins oblique or parallel to the regional schistosity in the Bt and Ms-Crd zones (Mateen et al., 2015; Terabayashi et al., 2010). This could have promoted deposition of highly crystalline hydrothermal graphite and could explain the high R2 values observed next to granitoids, but not the discrepancy between ΔS1 and R2.

8.3.3. Heating duration

Mori et al. (2017) showed that short-lived (10^2 years) heating by less than 100 m-thick intrusions can noticeably decrease the R2 ratio of CM but is not sufficient to reach steady-state CM crystallinity. Steady state appears to be attained in contact metamorphic aureoles around larger plutons, with modelled heating time scales of about 10^5 years (e.g. Hilchie and Jamieson, 2014). Nakamura et al. (2017) additionally attempted to extrapolate the kinetics of graphitization for a sample from the Hidaka belt (NE Japan), a high-T area similar to the Ryoke belt. Their figure 11 indicates that, at ~500 °C, the d_{002} of ideal graphite is attained much faster (10^6 years) than the complete elimination of in-plane defects (>10^8 years). These experimental results could suitably explain the discrepancy between higher out-of-plane and lower in-plane crystallinity.

8.3.4. Pressure

Both tectonic stress and lithostatic loading have a unit of pressure. As such, they are able to decrease the microporosity of natural CM and

assist graphitization (e.g. Blackman and Ubbelohde, 1962; Bonijoly et al., 1982; Deurbergue et al., 1987; Nakamura et al., 2020; Noda and Inagaki, 1962; Ross and Bustin, 1990). Beyssac et al. (2003a) similarly shows that S1 band splitting is favored by higher hydrostatic pressure or longer heating duration. Previous geobarometry in the study area documents distinct steps in pressure between the Chl–Bt (~1 kbar), Ms–Crd (~ 2 kbar) and Kfs–Crd (~ 2.5 kbar) zones (Kouketsu et al., 2014b), which could explain the stepwise increase of the out-of-plane parameters ΔS1 and L_c (Figs. 7c, 10a). The DP1 phase was associated with the foliation-parallel growth of metamorphic minerals in both the schist and gneiss zones, which also points to pervasive tectonic stress, in agreement with the recognition of regional flattening strain patterns in the area (Okudaira et al., 2009; Okudaira and Beppu, 2008).

8.3.5. Energetic considerations

An important result of some TEM studies about graphitization is that the transformation of CM starts with L_c increase *followed* by L_a increase (e.g. Rouzaud et al., 1983; Rouzaud and Oberlin, 1989). This is explained by the energy required to remove interstitial defects being lower than that required for the coalescence of adjacent crystallites and the removal of in-plane defects. Of the factors discussed above, only heating duration and pressure (1) provide additional energy during graphitization and (2) operate at a regional scale. However, a longer heating duration will tend to durably change both in-plane and out-of-plane CM crystallinity (Nakamura et al., 2017). Therefore, it is likely a combination of moderate temperature (~500 °C), non-protracted heating (10^6 years) and increased pressure (tectonic stress and/or lithostatic loading) that can explain the discrepancy between first- and second-order Raman data. These conditions were met on a regional scale in the Bt and Ms–Crd zones during the DP1 event.

9. Conclusions

A Raman spectroscopy study of carbonaceous material affected by successive contact and regional metamorphic events reveals that the combination of first- and second-order spectra can help constraining the tectono-thermal history of complex metamorphic terrains.

– As a complement to RSCM thermometry based on the first-order spectrum, a rapid inspection of the second-order S1 band should allow tracing the 500 °C isotherm and distinguishing between H–N–O–S-bearing (single S1) and C-richer (split S1) CM in metamorphic belts.
– RSCM thermometry is able to confidently reveal the influence of post-regional contact metamorphism. Delayed CM recrystallization can alter this potential, and likely depends on the crystallinity of the regionally-metamorphosed CM precursor.
– The ΔS1 parameter is calculated from peak splitting of the second-order S1 band; in addition to graphitization temperature, ΔS1 appears useful for tracing regional variations in heating duration and pressure.

Declaration of Competing Interest

None.

Gallhofer and C. Hauzenberger are thanked for reading an early version of the manuscript. Critical assessment of a previous version of the manuscript by two anonymous referees, review comments by Y. Kouketsu and Y. Nakamura, and editorial handling by M. Scambelluri are kindly acknowledged.

Appendix A. Parameters used for interpolated maps of T_{CM} and $\Delta S1$

Interpolated maps of T_{CM} and $\Delta S1$ presented in Fig. 8a, b were calculated with the same parameters for direct comparison. Interpolation was performed with the inverse distance weighting method (GRASS GIS module v.surf.idw; GRASS Development Team, 2017) and the following input parameters: number of interpolation points = 10 (out of 32 for T_{CM} and 30 for $\Delta S1$), power parameter = 2 (squared weighting), output pixel size = 45 m (~ 1/100 of the average distance between data points).

References

Akasaki, E., Owada, M., Kamei, A., 2015. Crustal differentiation due to partial melting of granitic rocks in an active continental margin, the Ryoke Belt, Southwest Japan. Lithos 230, 82–91.

Aoya, M., Kouketsu, Y., Endo, S., Shimizu, H., Mizukami, T., Nakamura, D., Wallis, S., 2010. Extending the applicability of the Raman carbonaceous-material geothermometer using data from contact metamorphic rocks. J. Metamorph. Geol. 28, 895–914.

Arruebarrena de Báez, M., Hendra, P.J., Judkins, M., 1995. The Raman spectra of oriented isotactic polypropylene. Spectrochim. Acta A Mol. Biomol. Spectrosc. 51, 2117–2124.

Bénny-Bassez, C., Rouzaud, J.N., 1985. Characterization of carbonaceous materials by correlated electron and optical microscopy and Raman microspectrometry. Scan. Electron Microsc. 1, 119–132.

Bernard, S., Beyssac, O., Benzerara, K., Findling, N., Tzvetkov, G., Brown, G.E., 2010. XANES, Raman and XRD study of anthracene-based cokes and saccharose-based chars submitted to high-temperature pyrolysis. Carbon 48, 2506–2516.

Beyssac, O., Lazzeri, M., 2012. Application of Raman spectroscopy to the study of graphitic carbons in the Earth Sciences. Applications of Raman spectroscopy to earth sciences and cultural heritage. EMU Notes Mineral. 12, 415–454.

Beyssac, O., Goffé, B., Chopin, C., Rouzaud, J.N., 2002a. Raman spectra of carbonaceous material in metasediments: a new geothermometer. J. Metamorph. Geol. 20, 859–871.

Beyssac, O., Rouzaud, J.-N., Goffé, B., Brunet, F., Chopin, C., 2002b. Graphitization in a high-pressure, low-temperature metamorphic gradient: a Raman microspectroscopy and HRTEM study. Contrib. Mineral. Petrol. 143, 19–31.

Beyssac, O., Brunet, F., Petitet, J.-P., Goffé, B., Rouzaud, J.-N., 2003a. Experimental study of the microtextural and structural transformations of carbonaceous materials under pressure and temperature. Eur. J. Mineral. 15, 937–951.

Beyssac, O., Goffé, B., Petitet, J.-P., Froigneux, E., Moreau, M., Rouzaud, J.-N., 2003b. On the characterization of disordered and heterogeneous carbonaceous materials by Raman spectroscopy. Spectrochim. Acta A Mol. Biomol. Spectrosc. 59, 2267–2276.

Beyssac, O., Pattison, D.R.M., Bourdelle, F., 2019. Contrasting degrees of recrystallization of carbonaceous material in the Nelson aureole, British Columbia and Ballachulish aureole, Scotland, with implications for thermometry based on Raman spectroscopy of carbonaceous material. J. Metamorph. Geol. 37, 71–95.

Beyssac, Olivier, Rouzaud, J.-N., Goffé, B., Brunet, F., Chopin, C., 2002. Graphitization in a high-pressure, low-temperature metamorphic gradient: a Raman microspectroscopy and HRTEM study. Contrib. Mineral. Petrol. 143, 19–31.

Blackman, L.C.F., Ubbelohde, A.R.J.P., 1962. Stress recrystallization of graphite. Proc. R. Soc. Lond. Ser. A. Math. Phys. Sci. 266, 20–32.

Bonijoly, M., Oberlin, M., Oberlin, A., 1982. A possible mechanism for natural graphite formation. Int. J. Coal Geol. 1, 283–312.

Brown, M., 1993. P-T-t evolution of orogenic belts and the causes of regional metamorphism. J. Geol. Soc. Lond. 150, 227–241.

Brown, M., 1998. Unpairing metamorphic belts: P-T paths and a tectonic model for the Ryoke Belt, Southwest Japan. J. Metamorph. Geol. 16, 3–22.

Buseck, P.R., Beyssac, O., 2014. From organic matter to graphite: graphitization. Elements 10, 421–426.

Buseck, P.R., Huang, B.-J., 1985. Conversion of carbonaceous material to graphite during metamorphism. Geochim. Cosmochim. Acta 49, 2003–2016.

Buseck, P.R., Huang, B., Keller, L.P., 1987. Electron microscope investigation of the structures of annealed carbons. Energy Fuel 1, 105–110.

Cançado, L.G., Takai, K., Enoki, T., Endo, M., Kim, Y.A., Mizusaki, H., Speziali, N.L., Jorio, A., Pimenta, M.A., 2008. Measuring the degree of stacking order in graphite by Raman spectroscopy. Carbon 46, 272–275.

Delchini, S., Lahfid, A., Plunder, A., Michard, A., 2016. Applicability of the RSCM geothermometry approach in a complex tectono-metamorphic context: the Jebilet massif case study (Variscan Belt, Morocco). Lithos 256–257, 1–12.

Deurbergue, A., Oberlin, A., Oh, J.H., Rouzaud, J.N., 1987. Graphitization of Korean anthracites as studied by transmission electron microscopy and X-ray diffraction. Int. J. Coal Geol. 8, 375–393.

Dresselhaus, M.S., Dresselhaus, G., Eklund, P.C., Chung, D.D.L., 1977. Lattice vibrations in graphite and intercalation compounds of graphite. Mater. Sci. Eng. 31, 141–152.

Ferrari, A.C., Robertson, J., 2000. Interpretation of Raman spectra of disordered and amorphous carbon. Phys. Rev. B 61, 14095–14107.

Ferrari, A.C., Meyer, J.C., Scardaci, V., Casiraghi, C., Lazzeri, M., Mauri, F., Piscanec, S., Jiang, D., Novoselov, K.S., Roth, S., Geim, A.K., 2006. Raman spectrum of graphene and graphene layers. Phys. Rev. Lett. 97, 187401.

Fischbach, D.B., 1970. The graphitization process. Tanso 63, 115–120.

Franklin, R.E., 1951. Crystallite growth in graphitizing and non-graphitizing carbons. Proc. R. Soc. Lond. Ser A. Math. Phys. Sci. 209, 196–218.

French, B.M., 1964. Graphitization of organic material in a progressively metamorphosed precambrian iron formation. Science 146, 917–918.

Geological Survey of Japan, 2012. Seamless digital geological map of Japan 1: 200,000. July 3, 2012 version. National Institute of Advanced Industrial Science and Technology (Ed.).

Geological Survey of Japan, 2013. Gravity Database of Japan. DVD edition, Digital Geoscience Map P-2. National Institute of Advanced Industrial Science and Technology (Ed.).

GRASS Development Team, 2017. Geographic Resources Analysis support System (GRASS) Software, Version 7.2. Open Source Geospatial Foundation. Electronic document. http://grass.osgeo.org.

Grew, E.S., 1974. Carbonaceous material in some metamorphic rocks of New England and other areas. J. Geol. 82, 50–73.

Griffin, G.M., 1967. X-ray diffraction techniques applicable to studies of diagenesis and low rank metamorphism in humic sediments. J. Sediment. Res. 37, 1006–1011.

Henry, D.G., Jarvis, I., Gillmore, G., Stephenson, M., 2019. Raman spectroscopy as a tool to determine the thermal maturity of organic matter: Application to sedimentary, metamorphic and structural geology. Earth Sci. Rev. 198, 102936.

Higashimoto, S., Nureki, T., Hara, I., Tsukuda, E., Nakajima, T., 1983. Geology of the Iwakuni district. Quadrangle Series, Scale 1:50,000, Geological Survey of Japan, p. 79.

Hilchie, L.J., Jamieson, R.A., 2014. Graphite thermometry in a low-pressure contact aureole, Halifax, Nova Scotia. Lithos 208–209, 21–33.

Hokada, T., 1998. Phase relations and P–T conditions of the Ryoke pelitic and psammitic metamorphic rocks in the Ina district, Central Japan. Island Arc 7, 609–620.

Ikeda, T., 1992. Prograde and Retrograde Metamorphisms of the Ryoke Belt in the Yanai District, Southwest Japan. Ph.D. Thesis. Kyoto University.

Ikeda, T., 1993. Compositional zoning patterns of garnet during prograde metamorphism from the Yanai district, Ryoke metamorphic belt, Southwest Japan. Lithos 30, 109–121.

Ikeda, T., 1998. Progressive sequence of reactions of the Ryoke metamorphism in the Yanai district, Southwest Japan: the formation of cordierite. J. Metamorph. Geol. 16, 39–52.

Ikeda, T., 2004. Pressure-temperature conditions of the Ryoke metamorphic rocks in Yanai district, SW Japan. Contrib. Mineral. Petrol. 146, 577–589.

Inagaki, M., 1996. Carbon materials Structure, texture and intercalation. Solid State Ionics 86–88, 833–839.

Ishihara, S., 1977. The magnetite-series and ilmenite-series granitic rocks. Min. Geol. 27, 293–305.

Itaya, T., 1981. Carbonaceous material in pelitic schists of the Sanbagawa metamorphic belt in Central Shikoku, Japan. Lithos 14, 215–224.

Izawa, E., 1968. Carbonaceous matter in some metamorphic rocks in Japan. J. Geol. Soc. Japan 74, 427–432.

Kawakami, T., 2001. Tourmaline breakdown in the migmatite zone of the Ryoke metamorphic belt, SW Japan. J. Metamorph. Geol. 19, 61–75.

Knight, D.S., White, W.B., 1989. Characterization of diamond films by Raman spectroscopy. J. Mater. Res. 4, 385–393.

Komazawa, M., 2013. Gravity Grid Data of Japan, Gravity Database of Japan, DVD edition. Digital Geoscience Map P-2. National Institute of Advanced Industrial Science and Technology (Ed.).

Kouketsu, Y., Mizukami, T., Mori, H., Endo, S., Aoya, M., Hara, H., Nakamura, D., Wallis, S., 2014a. A new approach to develop the Raman carbonaceous material geothermometer for low-grade metamorphism using peak width. Island Arc 23, 33–50.

Kouketsu, Y., Nishiyama, T., Ikeda, T., Enami, M., 2014b. Evaluation of residual pressure in an inclusion-host system using negative frequency shift of quartz Raman spectra. Am. Mineral. 99, 433–442.

Kouketsu, Y., Tsai, C.-H., Enami, M., 2019. Discovery of unusual metamorphic temperatures in the Yuli belt, eastern Taiwan: New interpretation of data by Raman carbonaceous material geothermometry. Geology 47, 522–526.

Kretz, R., 1983. Symbols for rock-forming minerals. Am. Mineral. 68, 277–279.

Kříbek, B., Sýkorová, I., Machovič, V., Laufek, F., 2008. Graphitization of organic matter and fluid-deposited graphite in Palaeoproterozoic (Birimian) black shales of the Kaya-Goren greenstone belt (Burkina Faso, West Africa). J. Metamorph. Geol. 26, 937–958.

Kwiecińska, B., Petersen, H.I., 2004. Graphite, semi-graphite, natural coke, and natural char classification—ICCP system. Int. J. Coal Geol. 57, 99–116.

Lahfid, A., Beyssac, O., Deville, E., Negro, F., Chopin, C., Goffé, B., 2010. Evolution of the Raman spectrum of carbonaceous material in low-grade metasediments of the Glarus Alps (Switzerland). Terra Nova 22, 354–360.

Landis, C.A., 1971. Graphitization of dispersed carbonaceous material in metamorphic rocks. Contrib. Mineral. Petrol. 30, 34–45.

Large, D.J., Christy, A.G., Fallick, A.E., 1994. Poorly crystalline carbonaceous matter in high grade metasediments: implications for graphitisation and metamorphic fluid compositions. Contrib. Mineral. Petrol. 116, 108–116.

Lespade, P., Marchand, A., Couzi, M., Cruege, F., 1984. Caracterisation de materiaux carbones par microspectrometrie Raman. Carbon 22, 375–385.

Malard, L.M., Pimenta, M.A., Dresselhaus, G., Dresselhaus, M.S., 2009. Raman spectroscopy in graphene. Phys. Rep. 473, 51–87.

Mateen, T., Yamamoto, H., Rehman, H.U., Terabayashi, M., 2015. Ductility contrast induced by silicification in pelitic schist of the Ryoke metamorphic belt, Japan. J. Struct. Geol. 80, 38–46.

Mateen, T., Okamoto, K., Chung, S.-L., Wang, K.-L., Lee, H.-Y., Abe, S., Mita, Y., Rehman, H.U., Terabayashi, M., Yamamoto, H., 2019. LA-ICP-MS zircon U-Pb age and Hf isotope data from the granitic rocks in the Iwakuni area, Southwest Japan: re-evaluation of emplacement order and the source magma. Geosci. J. 23, 917–931.

Miyazaki, K., 2010. Development of migmatites and the role of viscous segregation in high-T metamorphic complexes: example from the Ryoke Metamorphic complex, Mikawa Plateau, Central Japan. Lithos 116, 287–299.

Mori, H., Mori, N., Wallis, S., Westaway, R., Annen, C., 2017. The importance of heating duration for Raman CM thermometry: evidence from contact metamorphism around the Great Whin Sill intrusion, UK. J. Metamorph. Geol. 35, 165–180.

Nakajima, T., 1994. The Ryoke plutonometamorphic belt: crustal section of the cretaceous Eurasian continental margin. Lithos 33, 51–66.

Nakajima, T., Shirahase, T., Shibata, K., 1990. Along-arc lateral variation of Rb−Sr and K −Ar ages of cretaceous granitic rocks in Southwest Japan. Contrib. Mineral. Petrol. 104, 381–389.

Nakajima, T., Horie, K., Adachi, T., Miyazaki, K., Dunkley, D.J., Hokada, T., 2013. SHRIMP U-Pb Ages of Zircons from Ryoke Metamorphic Rocks. Geological Society of Japan Annual Meeting, Abstract Volume, p. 51.

Nakajima, T., Takahashi, M., Imaoka, T., Shimura, T., 2016. Granitic rocks. In: Moreno, T., Wallis, S., Kojima, T., Gibbons, W. (Eds.), The Geology of Japan. Geological Society London, pp. 251–272.

Nakamura, D., 1995. Comparison and interpretation of graphitization in contact and regional metamorphic rocks. Island Arc 4, 112–127.

Nakamura, Y., Akai, J., 2013. Microstructural evolution of carbonaceous material during graphitization in the Gyoja-yama contact aureole: HRTEM, XRD and Raman spectroscopic study. J. Mineral. Petrol. Sci. 108, 131–143.

Nakamura, Y., Yoshino, T., Satish-Kumar, M., 2017. An experimental kinetic study on the structural evolution of natural carbonaceous material to graphite. Am. Mineral. 102, 135–148.

Nakamura, Y., Yoshino, T., Satish-Kumar, M., 2020. Pressure dependence of graphitization: implications for rapid recrystallization of carbonaceous material in a subduction zone. Contrib. Mineral. Petrol. 175, 32.

Nemanich, R.J., Solin, S.A., 1979. First- and second-order Raman scattering from finite-size crystals of graphite. Phys. Rev. B 20, 392–401.

Noda, T., Inagaki, M., 1962. Heat Treatment of Carbon under various pressures. Nature 196, 772.

Nureki, T., 1974. Contact metamorphism in the So-o district, Yamaguchi Prefecture, Japan - with special reference to the occurrence of sillimanite. Mem. Geol. Soc. Japan 11, 251–281.

Okudaira, T., Beppu, Y., 2008. Inhomogeneous deformation of metamorphic tectonites of contrasting lithologies: Strain analysis of metapelite and metachert from the Ryoke metamorphic belt, SW Japan. J. Struct. Geol. 30, 39–49.

Okudaira, T., Hara, I., Takeshita, T., 1995. Emplacement mechanism of the older Ryoke granites in the Yanai district, Southwest Japan, with special reference to extensional deformation in the Ryoke metamorphic belt. J. Sci. Hiroshima Univ. Ser. C 10, 357–366.

Okudaira, T., Beppu, Y., Yano, R., Tsuyama, M., Ishii, K., 2009. Mid-crustal horizontal shear zone in the forearc region of the mid-cretaceous SW Japan arc, inferred from strain analysis of rocks within the Ryoke metamorphic belt. J. Asian Earth Sci. 35, 34–44.

Pasteris, J.D., Wopenka, B., 1991. Raman spectra of graphite as indicators of degree of metamorphism. Can. Mineral. 29, 1–9.

Pattison, D.R.M., Tracy, R.J., 1991. Phase equilibria and thermobarometry of metapelites. Rev. Mineral. Geochem. 26, 105–206.

Pimenta, M.A., Dresselhaus, G., Dresselhaus, M.S., Cançado, L.G., Jorio, A., Saito, R., 2007. Studying disorder in graphite-based systems by Raman spectroscopy. Phys. Chem. Chem. Phys. 9, 1276–1290.

Pócsik, I., Hundhausen, M., Koós, M., Ley, L., 1998. Origin of the D peak in the Raman spectrum of microcrystalline graphite. J. Non-Cryst. Solids 227–230, 1083–1086.

Rahl, J.M., Anderson, K.M., Brandon, M.T., Fassoulas, C., 2005. Raman spectroscopic carbonaceous material thermometry of low-grade metamorphic rocks: Calibration and application to tectonic exhumation in Crete, Greece. Earth Planet. Sci. Lett. 240, 339–354.

Reich, S., Thomsen, C., 2004. Raman spectroscopy of graphite. Phil. Trans. R. Soc. Lond., p. 362.

Ross, J.V., Bustin, R.M., 1990. The role of strain energy in creep graphitization of anthracite. Nature 343, 58–60.

Rouzaud, J.N., Oberlin, A., 1989. Structure, microtexture, and optical properties of anthracene and saccharose-based carbons. Carbon 27, 517–529.

Rouzaud, J.N., Oberlin, A., Beny-Bassez, C., 1983. Carbon films: structure and microtexture (optical and electron microscopy, Raman spectroscopy). Thin Solid Films 105, 75–96.

Sato, H., 1933. Yanaizu Geological Map, 1:75 000. Imperial Geological Survey of Japan.

Sato, K., Saito, R., Oyama, Y., Jiang, J., Cançado, L.G., Pimenta, M.A., Jorio, A., Samsonidze, G.G., Dresselhaus, G., Dresselhaus, M.S., 2006. D-band Raman intensity of graphitic materials as a function of laser energy and crystallite size. Chem. Phys. Lett. 427, 117–121.

Sinha, K., Menéndez, J., 1990. First- and second-order resonant Raman scattering in graphite. Phys. Rev. B 41, 10845–10847.

Skrzypek, E., Kawakami, T., Hirajima, T., Sakata, S., Hirata, T., Ikeda, T., 2016. Revisiting the high temperature metamorphic field gradient of the Ryoke Belt (SW Japan): new constraints from the Iwakuni-Yanai area. Lithos 260, 9–27.

Skrzypek, E., Kato, T., Kawakami, T., Sakata, S., Hattori, K., Hirata, T., Ikeda, T., 2018. Monazite behaviour and time-scale of metamorphic processes along a low-pressure/high-temperature field gradient (Ryoke Belt, SW Japan). J. Petrol. 59, 1109–1144.

Skrzypek, E., Sakata, S., Sorger, D., 2020. Alteration of magmatic monazite in granitoids from the Ryoke belt (SW Japan): processes and consequences. Am. Mineral. 105, 538–554.

Sugawara, Y., 2013. Thermobaric Structure in the Low pressure/Temperature Type Ryoke Metamorphic Belt and its Implications for Crustal Evolution. Ph.D. Thesis, Kyushu University.

Tagiri, M., 1981. A measurement of the graphitizing-degree by the X-Ray powder diffractometer. J. Japan. Assoc. Mineral. Petrol. Econom. Geol. 76, 345–352.

Takami, M., Isozaki, Y., Nishimura, Y., Itaya, T., 1993. Effect of detrital white mica and contact metamorphism to K-Ar dating of weakly metamorophosed accretionary complex:an example of Jurassic accretionary complex in eastern Yamaguchi Prefecture, Southwest Japan. J. Geol. Soc. Japan 99, 545–563.

Terabayashi, M., Yamamoto, H., Hiwatashi, E., Kitajima, K., 2010. Silicification of pelitic schist in the Ryoke low-pressure/temperature metamorphic belt, Southwest Japan: origin of competent layers in the middle crust: Competent layers in middle crust. Island Arc 19, 17–29.

Thomsen, C., Reich, S., 2000. Double Resonant Raman Scattering in Graphite. Phys. Rev. Lett. 85, 5214–5217.

Tsuchiya, N., Suzuki, S., Oda, Y., 1987. Thermal effect of Granite Pluton on Graphitization of Carbonaceous Material in the Kuga Group, Southwest Japan. J. Japan. Assoc. Mineral. Petrol. Econom. Geol. 82, 362–369.

Tuinstra, F., Koenig, J.L., 1970. Raman spectrum of graphite. J. Chem. Phys. 53, 1126–1130.

Vidano, R.P., Fischbach, D.B., Willis, L.J., Loehr, T.M., 1981. Observation of Raman band shifting with excitation wavelength for carbons and graphites. Solid State Commun. 39, 341–344.

Wada, H., Tomita, T., Matsuura, K., Tuchi, K., Ito, M., Morikiyo, T., 1994. Graphitization of carbonaceous matter during metamorphism with references to carbonate and pelitic rocks of contact and regional metamorphisms, Japan. Contrib. Mineral. Petrol. 118, 217–228.

Wallis, S.R., Okudaira, T., 2016. Paired metamorphic belts of SW Japan: The geology of the Sanbagawa and Ryoke metamorphic belts and the median Tectonic Line. In: Moreno, T., Wallis, S., Kojima, T., Gibbons, W. (Eds.), The Geology of Japan. Geological Society London, pp. 101–124.

Wang, G.-F., 1989. Carbonaceous material in the Ryoke metamorphic rocks, Kinki district, Japan. Lithos 22, 305–316.

Wilhelm, H., Lelaurain, M., McRae, E., Humbert, B., 1998. Raman spectroscopic studies on well-defined carbonaceous materials of strong two-dimensional character. J. Appl. Phys. 84, 6552–6558.

Wintsch, R.P., O'Connell, A.F., Ransom, B.L., Wiechmann, M.J., 1981. Evidence for the influence of fCH4 on the crystallinity of disseminated carbon in greenschist facies rocks, Rhode Island, USA. Contrib. Mineral. Petrol. 77, 207–213.

Wojdyr, M., 2010. Fityk: a general-purpose peak fitting program. J. Appl. Crystallogr. 43, 1126–1128.

Wopenka, B., Pasteris, J.D., 1993. Structural characterization of kerogens to granulite-facies graphite: Applicability of Raman microprobe spectroscopy. Am. Mineral. 78, 533–557.